Journal of Materials Chemistry A

Accepted Manuscript

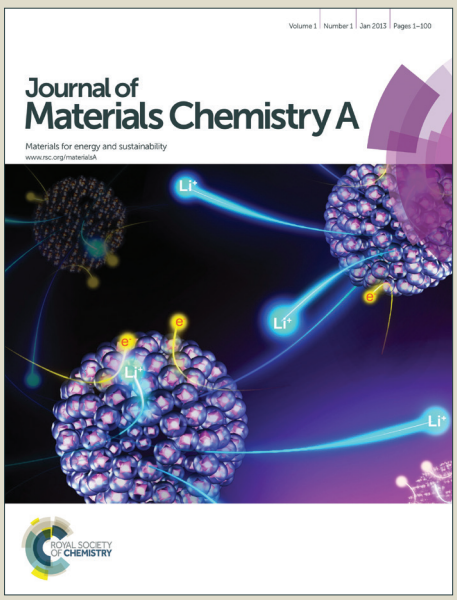

ROYAL SOCIETY OF CHEMISTRY

www.rsc.org/materialsA

Graphical and textual abstract

Hierarchical $NiFe_2O_4/Fe_2O_3$ nanotubes derived from metal organic frameworks for superior lithium ion battery anode

Gang Huang[ac], Feifei Zhang[ac], Leilei Zhang[ac], Xinchuan Du[ac], Jianwei Wang[ac] and Limin Wang[ab]*

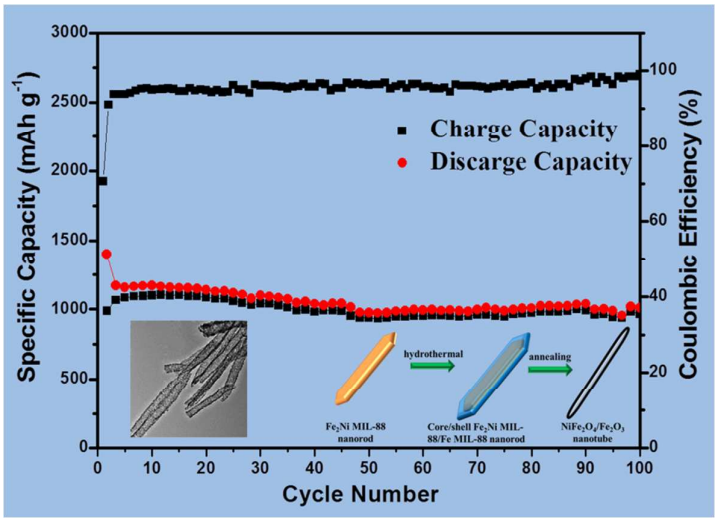

Core/shell MOFs templated synthesis of porous $NiFe_2O_4@Fe_2O_3$ nanotubes exhibit large reversible capacity, excellent cyclic stability and superior rate capability as anode materials for Li-ion battery.

Journal Name

RSCPublishing

ARTICLE

Hierarchical $NiFe_2O_4/Fe_2O_3$ nanotubes derived from metal organic frameworks for superior lithium ion battery anode

Cite this: DOI: 10.1039/xoxxoooooox

Received ooth January 2012,
Accepted ooth January 2012

DOI: 10.1039/xoxxoooooox

www.rsc.org/

Gang Huang[ac], Feifei Zhang[ac], Leilei Zhang[ac], Xinchuan Du[ac], Jianwei Wang[ac] and Limin Wang[ab]*

A simple method for the synthesis of $NiFe_2O_4/Fe_2O_3$ nanotubes by annealing core/shell metal organic frameworks (MOFs) Fe_2Ni MIL-88/Fe MIL-88 has been developed. The crystalline phase, morphology and specific surface area (BET) of the resultant sample have been systematically characterized. The results indicate that the $NiFe_2O_4/Fe_2O_3$ nanotubes with diameters of 78 nm and lengths up to around 1 μm are composed of nano-sized primary particles. The electrochemical performance of $NiFe_2O_4/Fe_2O_3$ nanotubes as anode materials for lithium ion batteries has been tested. A reversible specific capacity of 936.9 mAh g^{-1} is achieved at a current density of 100 mA g^{-1} up to 100 cycles. Even at 2000 mA g^{-1}, the discharge capacity of the composite anode could still be reached 423.6 mAh g^{-1}. The enhanced electrochemical performance of the $NiFe_2O_4/Fe_2O_3$ nanotubes anode is ascribed to the rational design of the hierarchical porous hollow structures and the synergetic effect of different functional components.

Introduction

Lithium ion batteries (LIBs) have been regarded as one of the most promising green and clean renewable energy sources and widely used in portable consumer electronics.[1,2] Recently, there have been aroused dramatic demands for LIBs with higher energy density, better rate capability and longer cycling life, especially for the newly emerging large scale applications, i.e. electric vehicles and grid storage. However, graphite, the most commercial used anode material, cannot meet this end due to its low capacity, poor rate performance and security issues. Owing to the high theoretical capacities, transition metal oxides, such as Fe_2O_3, Fe_3O_4, Co_3O_4 and Mn_3O_4, are widely studied.[3-6] Among them, Fe-base oxides have drawn considerable attention because of its low cost, non-toxicity and natural abundance.[7] Nevertheless, the pulverization of the electrode caused by the huge volume change during the lithiation and delithiation process, makes Fe-base oxides with rapid capacity degradation and poor cycling stability. There are different approaches to overcome this obstacle. One solution is to fabricate Fe-base oxides with novel structures, such as one-dimension porous hollow structures, which have large surface area and surface to volume ratio, affording facial transport pathways for both electrons and ions. In addition, the hollow structure can partially alleviate the stress of the electrode materials during the charge-discharge process.[8] Other solutions are to synthesize ternary compounds or assemble different oxides into hierarchical composite, such as $NiFe_2O_4$, $MnFe_2O_4$, $ZnFe_2O_4$, Fe_2O_3/MnO_2, Co_3O_4/Fe_2O_3 and Fe_2O_3/SnO_2, which can offer richer redox chemistry and combine the contributions from different components.[9-14] Thus, the electrochemical performance of the Fe-base oxides has been improved.

Metal organic frameworks (MOFs), synthesized by self-assembly of metal clusters and organic molecules into an infinite array, are a new class of porous materials and have shown promising applications in gas storage, catalysis, sensing and separations.[15-18] Motivated by the high surface area and unique structures, MOFs have been regarded as novel templates to prepare porous metal oxides.[19-21] As compared to other templates, MOFs exhibit distinct advantages in synthesizing metal oxides with tailorable function, large surface area and inter-connected pores. Most importantly, these MOFs derived metal oxides exhibit enhanced electrochemical performance when evaluated as anode materials for LIBs.[22-24] Despite of the great progress achieved so far, the research on the fabrication of multiple metal oxide composite from MOFs and their application as electrode materials for LIBs is still at early stage.

In this work, hierarchical $NiFe_2O_4/Fe_2O_3$ nanotubes have been simply synthesized by using core/shell Fe_2Ni MIL-88/Fe MIL-88 as template followed by a post-annealing process. When evaluated as anode materials for LIBs, the porous feature, hollow structure and synergetic effect of $NiFe_2O_4$ and Fe_2O_3 make the composite deliver excellent electrochemical performance.

Experimental

Synthesis of Fe_2Ni MIL-88 nanorods

All chemicals were directly used after purchase without any further purification. In a typical synthesis, 0.1811 g of $FeCl_3$ $6H_2O$, 0.096 g of $Ni(NO_3)_2$ $6H_2O$ and 0.1661 g of 1,4-benzenedicarboxylic acid (H_2bdc) were dissolved in 10 ml of DMF under stirring until the solution became clear. Then, 2 ml of 0.4 mol/L NaOH solution was added with continuous stirring for another 15 min. The mixture was then transferred into a Teflon-lined autoclave and heated at 100 ℃ for 15 h. The autoclave was allowed to cool to room temperature naturally. The solid product was recovered by centrifugation and washed several times with DMF and finally dried at 70 ℃ for 12 h.

Synthesis of core/shell Fe_2Ni MIL-88/Fe MIL-88 nanorods

In a typical synthesis, 60 mg of the as-prepared Fe_2Ni MIL-88 was first dispersed in 12 mL of DMF under ultrasonic condition for 10 min. Then 192 mg of $FeCl_3$ $6H_2O$, 90 mg of H_2bdc and 12 mL of CH_3CN were added to the above solution under stirring for 10 min. The mixture was then transferred into a Teflon-lined autoclave and heated at 120 ℃ for 1 h. The resulting product was isolated and subsequently washed with DMF and methanol via centrifugation-redispersion cycles and finally dried at 70 ℃ for 12 h.

Synthesis of $NiFe_2O_4/Fe_2O_3$ and $NiFe_2O_4$ nanotubes

The as-synthesized Fe_2Ni MIL-88/Fe MIL-88 was heated in air at 450 ℃ for 6 h with a temperate ramp of 2 ℃ min^{-1} to synthesize $NiFe_2O_4/Fe_2O_3$ nanotubes.

The $NiFe_2O_4$ nanotubes were obtained by annealing the as-prepared Fe_2Ni MIL-88 nanorods in air at 450 ℃ for 6 h.

Characterization

The Powder X-ray diffraction (XRD) patterns were collected by a Bruker D8 Focus power X-ray diffractometer with Cu Kα radiation at a scan rate of 2 ° min^{-1}. Scanning electron microscope (SEM) images were obtained on a Hitachi S-4800 field emission scanning electron microscope using an accelerating voltage of 10 kV. Transmission electron microscope (TEM), high-angle annular dark-field scanning transmission electron microscopy (HAADF-STEM), line scan Energy dispersive X-ray spectroscopy (EDS) elemental analysis and element mapping were performed on a FEI Tecnai G2 S-Twin instrument with a field emission gun operating at 200 kV. Thermogravimetric (TG) analysis was performed in air from 25 to 600 ℃ with a heating rate of 10 ℃ min^{-1} by using STA 449 Jupiter (NETZSCH) thermogravimetry analyser. N_2 adsorption-desorption measurements were conducted on a Micromeritics ASAP 2010 instrument at -196 ℃ after the sample was degassed at 150 ℃ for 6 h under the vacuum conditions.

Electrochemical measurements

The electrochemical behaviour of the $NiFe_2O_4/Fe_2O_3$ nanotubes was examined by using CR 2025 coin-type cells with pure lithium foil as the counter electrode, Celgard 2400 membrane as the separator, 1 M $LiPF_6$ dissolved in ethyl carbonate and diethyl carbonate (1:1, wt/wt) as the electrolyte. The working electrode was prepared by compressing a mixture of the active materials, carbon black and poly(vinylidene fluoride) with a weight ratio of 70: 20: 10 on to a copper foil and dried in a vacuum oven at 80 ℃ for 12 h. The mass loading of active material for the testing electrodes is about 1.0-1.2 mg. Then the cells were assembled in a glove box filled with highly pure argon gas. The charge-discharge performance was tested between 0.01-3 V, using the LAND CT2001A multi-channel battery testing system at room temperature. The cyclic voltammogram (CV) measurements were conducted on a CHI660C Electrochemical Workstation at a scan rate of 0.1 mV s^{-1} in a potential range of 0.01-3 V *vs.* Li/Li^+.

Results and discussion

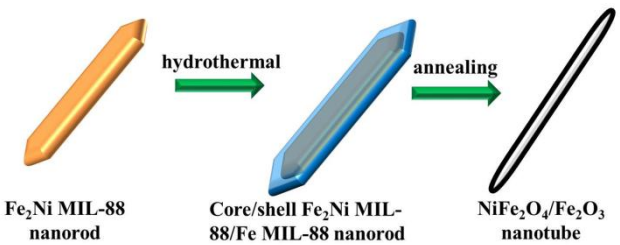

Fig. 1 Schematic illustration of the procedure used to fabricate $NiFe_2O_4/Fe_2O_3$ nanotubes.

Fig. 1 illustrates the overall strategy for the fabrication of hierarchical $NiFe_2O_4/Fe_2O_3$ nanotubes. Fe_2Ni MIL-88 nanorods are firstly synthesized *via* a hydrothermal method by using $FeCl_3$ $6H_2O$, $Ni(NO_3)_2$ $6H_2O$ and H_2bdc as precursors. The resulting Fe_2Ni MIL-88 is then used as seeds for the growth of a layer of Fe MIL-88 on the surface of it. Owing to the similar crystal structure and lattice constants of MIL-88 analogues, core/shell Fe_2Ni MIL-88/Fe MIL-88 nanorods have been successfully fabricated by the consecutive hydrothermal reaction of the Fe MIL-88 precursors ($FeCl_3$ $6H_2O$ and H_2bdc) in the presence of the initially formed Fe_2Ni MIL-88. Finally, an annealing treatment at 450 ℃ for 6 h is utilized to convert the core/shell composite into $NiFe_2O_4/Fe_2O_3$ nanotubes, which is mainly based on the nonequilibrium interdiffusion process.[21,22] At the initial stage of calcination, a thin intermediate shell with lots of vacancies forms on the surface of the composite. The vacancies in this thin shell can allow the outward diffusion of the Fe_2Ni MIL-88/Fe MIL-88 and inward diffusion of the atmospheric oxygen. Due to the faster diffusion rate of Fe_2Ni MIL-88/Fe MIL-88 than that of oxygen, hollow cavity is thus generated. Accompanied with the release of internally generated H_2O and CO_2 during the thermal decomposition process, hierarchical porous $NiFe_2O_4/Fe_2O_3$ nanotubes are eventually fabricated.

The crystal structure of Fe_2Ni MIL-88 is confirmed by the XRD patterns (Fig. S1), which are consistent with the previous reported literature.[25] The strong intensity and narrow peaks indicate that the as-synthesized Fe_2Ni MIL-88 is of high

crystallinity. As the SEM and TEM images shown in Fig. S2, the Fe_2Ni MIL-88 with a large-amount of nanorods turn out to be in good dispersity. Based on a statistical calculation of more than 50 nanorods, the mean diameter of the Fe_2Ni MIL-88 is deduced to be 91 nm. Then a layer of Fe MIL-88 is deposited on the surface of Fe_2Ni MIL-88, forming a core/shell structure. Fig. 2 gives the XRD patterns of the composite, except the peaks from Fe_2Ni MIL-88 phase, all other diffraction peaks can be readily indexed as Fe MIL-88, [25,26] indicating the successful synthesis of Fe_2Ni MIL-88/Fe MIL-88 composite.

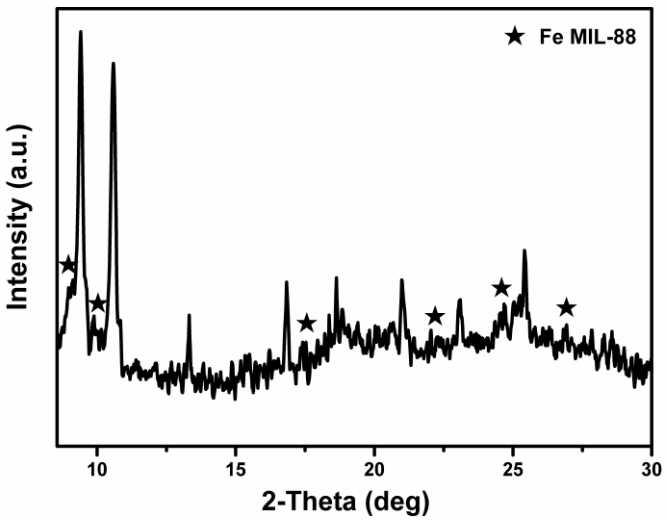

Fig. 2 XRD patterns of the as-prepared core/shell Fe_2Ni MIL-88/Fe MIL-88 nanorods.

The Fe MIL-88 depositing process does not bring any morphological change as confirmed by the SEM images shown in Fig. 3. The composite keeps the rod-shaped morphology with an average diameter of 124 nm. The increase in the size of the composite mainly contributes to the growth of a second layer on the surface of initial Fe_2Ni MIL-88 nanorods. TEM and line scan EDS analysis have been conducted to confirm the core/shell structure of the Fe_2Ni MIL-88/Fe MIL-88. Fig. 4a and Fig. 4b reveal that Fe MIL-88 with a shell thickness of around 16 nm uniformly covers the surface of the Fe_2Ni MIL-88 nanorods. As evidenced by the dominance of the Ni element at the center of the nanorod as a core component and the uniform distribution of Fe element across the entire nanorod, both as the shell and core component, the line scan EDS element analysis in Fig. 4c further confirms the core/shell structure of the composite. This leads us to conclude that the initial Fe_2Ni MIL-88 acts as seeds for the growth of Fe MIL-88 layer.

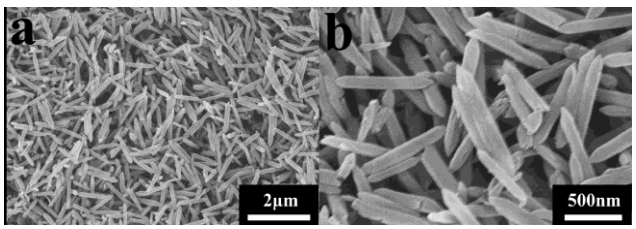

Fig. 3 SEM images of the as-synthesized Fe_2Ni MIL-88/Fe MIL-88 nanorods.

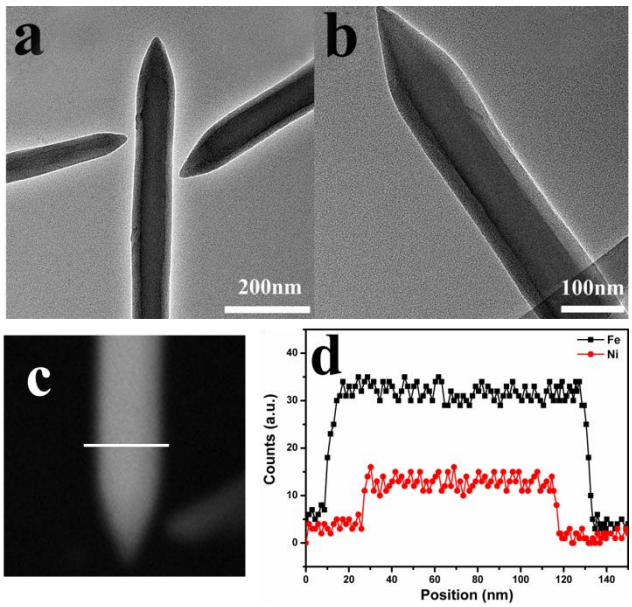

Fig. 4 (a) (b) TEM images (c) HAADF-STEM image and (d) line scan EDS element analysis of the as-prepared core/shell Fe_2Ni MIL-88/Fe MIL-88 nanorods.

The TG analysis gives us an insight into the thermal decomposition process of the core/shell Fe_2Ni MIL-88/Fe MIL-88 nanorods (Fig. S3). The first step with a weight loss of 13.62 wt% takes place between 25-300 ℃, which is ascribed to the removal of the adsorbed and coordinated water molecules. The subsequent heating at the temperature above 400 ℃ results in the complete decomposition of the core/shell composite with a cliffy weight loss of 58.07%, attributing to the oxidation of the organic linker into CO_2 and H_2O. As a result, 450 ℃ is chosen

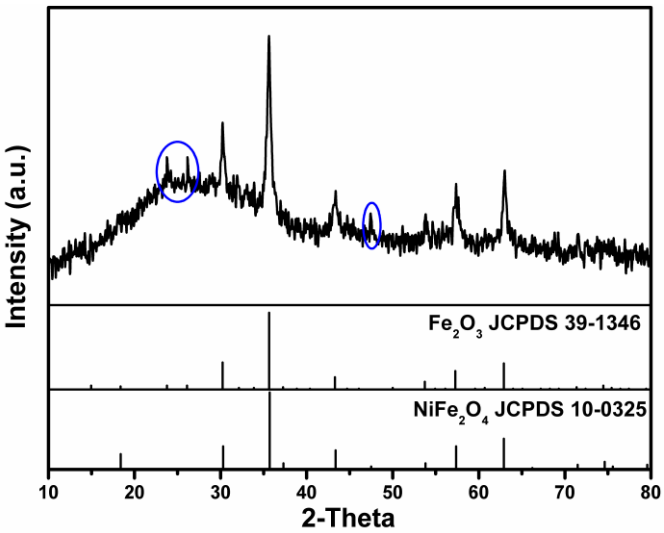

Fig. 5 XRD patterns of the as-synthesized $NiFe_2O_4/Fe_2O_3$ nanotubes.

as the calcinating temperature. The XRD patterns of the calcinating product are shown in Fig. 5, all the peaks can be assigned to the cubic spinel phase $NiFe_2O_4$ (JPCDF No. 10-0325) and rhombohedral Fe_2O_3 (JPCDF No. 39-1346) and no peaks from other crystalline byproducts can be identified. Because of the similar unit cell parameters of $NiFe_2O_4$ and

Fe_2O_3, and the broaden effect of the small particles, the diffraction peaks from the two phase cannot be easily distinguished. However, the presence of the $NiFe_2O_4$ phase can be inferred from the (331) reflection at 47.5°, while the (210), (211) reflections at 23.8° and 26.1° corresponding to the Fe_2O_3 phase are also visible, indicating the successful synthesis of $NiFe_2O_4/Fe_2O_3$ composite. Moreover, the comparison of the XRD patterns of $NiFe_2O_4/Fe_2O_3$ and $NiFe_2O_4$ (Fig. S5c) could further confirm the existence of $NiFe_2O_4$ and Fe_2O_3 in the thermal product.

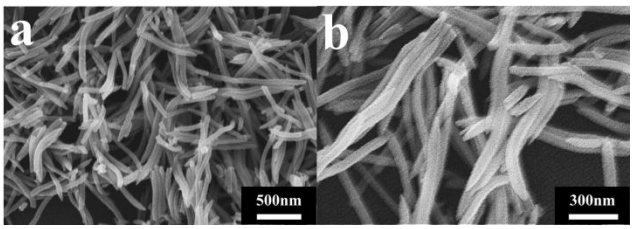

Fig. 6 SEM images of the as-synthesized $NiFe_2O_4/Fe_2O_3$ nanotubes.

The morphology of the $NiFe_2O_4/Fe_2O_3$ is characterized by the SEM images shown in Fig. 6. It can be observed that the nanorod structure is basically maintained after calcination, except that the nanorod changes from straight to curve and the size decreases, which is caused by the removing of organic part during calcination. The morphology and microstructure of the $NiFe_2O_4/Fe_2O_3$ are further examined by TEM and element mappings. Fig. 7a and Fig. 7b indicate that the $NiFe_2O_4/Fe_2O_3$ composite is nanotubes with diameter of approximately 78 nm and length of about 1μm. Moreover, the nanotubes are composed by nano-sized primary particles and exhibit a mesoporous feature. The element mappings in Fig. 7c reveal that Fe and Ni are well-distributed throughout the nanotube, implying the homogeneous mixing of $NiFe_2O_4$ and Fe_2O_3. In general, the conversion of core/shell Fe_2Ni MIL-88/Fe MIL-88 nanorods to $NiFe_2O_4/Fe_2O_3$ nanotubes is highly achievable by calcination.

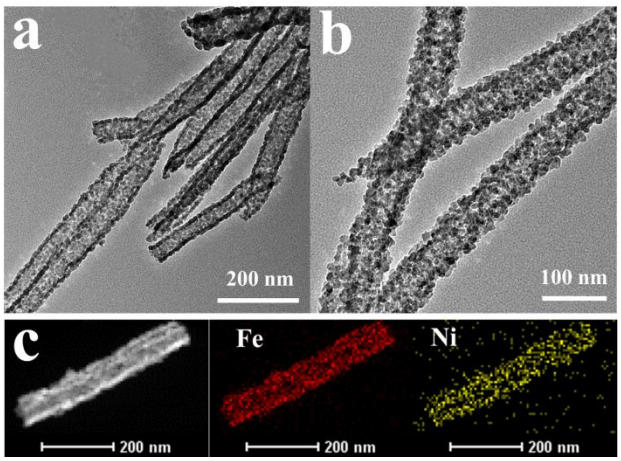

Fig. 7 (a) (b) TEM images (c) HAADF-STEM and Elemental mapping of $NiFe_2O_4/Fe_2O_3$ nanotubes.

N_2 adsorption-desorption analysis is performed to investigate the specific surface areas and pore-size distribution of the $NiFe_2O_4/Fe_2O_3$ nanotubes. As shown in Fig. S4a, the sorption isotherm exhibits type IV isotherm with a distinct hysteresis loop over the range of $0.7 < P/P_0 < 0.95$, indicating the typical mesopore characteristic of the $NiFe_2O_4/Fe_2O_3$. The BET surface areas and total pore volume of the $NiFe_2O_4/Fe_2O_3$ nanotubes are calculated to be 39.20 $m^2\ g^{-1}$ and 0.21 $cm^3\ g^{-1}$, respectively. A Barrett-Joyner-Halenda (BJH) calculation based on adsorption data exhibits that the sizes of most of the pores are around 17.67 nm (Fig. S4b). The large surface area endows the metal oxides with more lithium storage sites, while the mesoporous structure can effectively facilitate the transportation of the Li^+ and electrolyte molecules, and relieve the volume change of the electrode materials during the repeated charge-discharge process.

Inspired by the structures and composition advantages, the electrochemical performance of the $NiFe_2O_4/Fe_2O_3$ nanotubes as anode materials for LIBs has been evaluated by CV and galvanostatic charge-discharge measurement. Fig. 8a shows the initial three CV curves of the $NiFe_2O_4/Fe_2O_3$ electrode, which is obtained from 0.01-3 V at a scan rate of 0.1 mV s^{-1}. In the first cathodic sweep, the minuscule peak around 1.5 V represents the formation of hexagonal α-$Li_xFe_2O_3$,[27] while the intense peak around 0.62 V corresponds to the complete reduction of Ni^{2+}, Fe^{2+} and Fe^{3+} to Ni and Fe, and the formation of a solid electrolyte interface (SEI) film.[27] This peak is replaced by a broad peak at 0.8 V with decreased intensity in the subsequent cycle, suggesting the irreversible phase transformation in the first cycle. The small peak at 1.72 V might be ascribed to insertion of Li^+ to Fe_2O_3.[28,29] During the anodic process, the peak at 1.80 V corresponds to the reversible oxidation of Ni to Ni^{2+} and Fe to Fe^{3+}, respectively. The curves are well-overlapped after the first cycle, indicating the good electrochemical reversibility of the $NiFe_2O_4/Fe_2O_3$ nanotubes. Based on the CV results and the storage mechanisms of $NiFe_2O_4$ and Fe_2O_3,[3,9,27,30] the whole electrochemical reactions involved in the charge-discharge process are believed to be as follows:

$$NiFe_2O_4 + 8Li^+ + 8e^- \rightarrow Ni + 2Fe + 4Li_2O \quad (1)$$

$$Ni + Li_2O \leftrightarrow NiO + 2Li^+ + 2e^- \quad (2)$$

$$Fe_2O_3 + 6Li^+ + 8e^- \leftrightarrow 2Fe + 3Li_2O \quad (5)$$

The galvanostatic charge-discharge voltage profiles of the $NiFe_2O_4$ and $NiFe_2O_4/Fe_2O_3$ at a current density of 100 mA g^{-1} in the voltage range of 0.01-3 V are shown in Fig. S6a and Fig. 8a, respectively. In the first discharge process, both of the electrodes exhibit a small voltage plateau at 1.5 V and a long flat plateau at 0.8 V. For the subsequent discharge process, the potential plateau shifts upward to about 1.0 V due to the structural reorganization, new phase formation and the polarization change of the electrode material,[31,32] which agrees well with the CV results. The initial discharge and charge

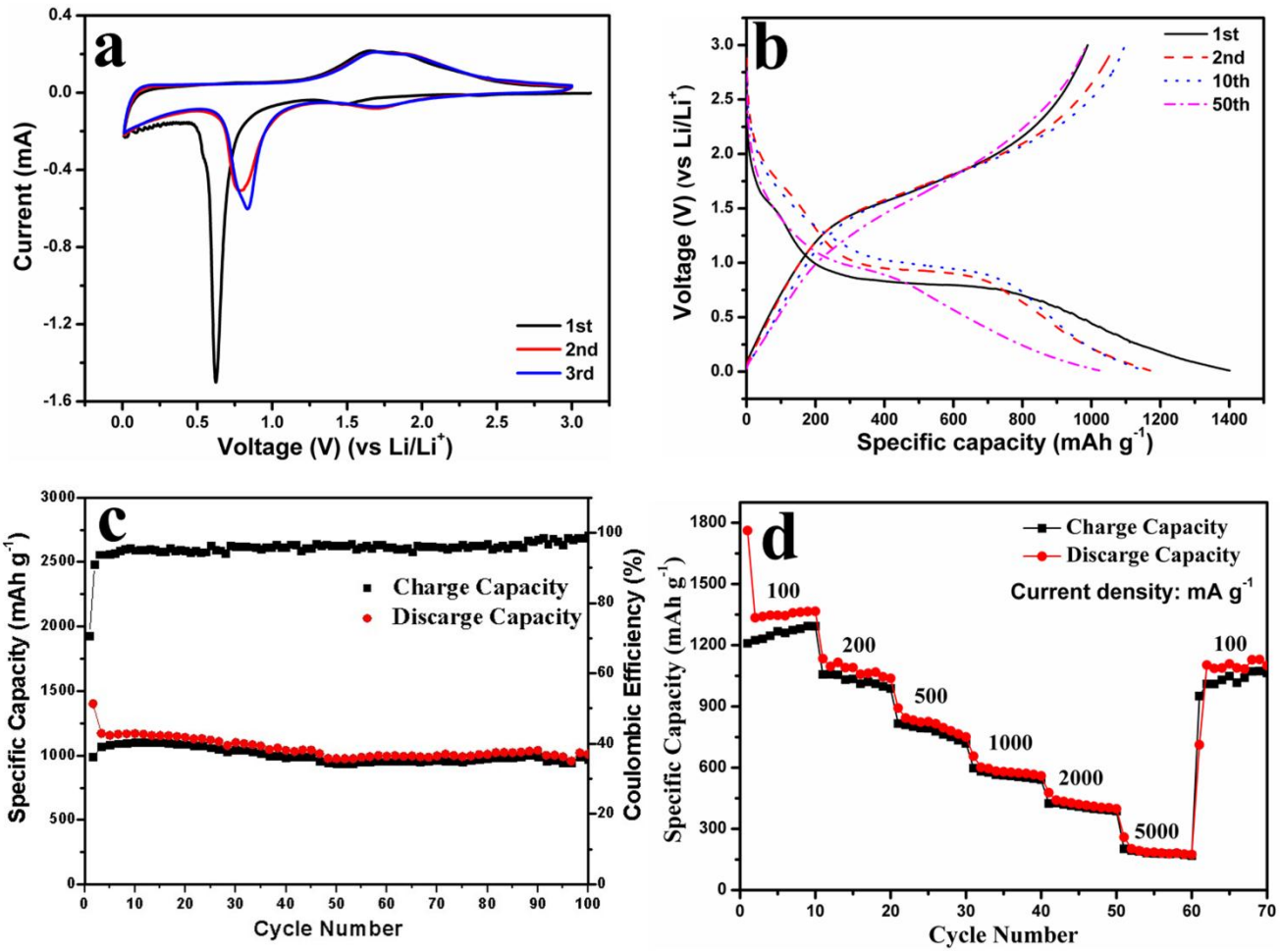

Fig. 8 (a) Representative cyclic voltammograms (CVs) of the $NiFe_2O_4/Fe_2O_3$ nanotubes at a scan rate of 0.1 mV s^{-1} between 0.01-3 V *vs.* Li/Li^+. (b) Charge–discharge voltage profiles of the $NiFe_2O_4/Fe_2O_3$ nanotubes for the 1st, 2nd, 10th and 50th cycles in the voltage range of 0.01-3 V at a current rate of 100 mA g^{-1}. (c) Capacity and Coulombic efficiency *vs*. cycle number of the $NiFe_2O_4/Fe_2O_3$ nanotubes at a current rate of 100 mA g^{-1}. (d) Rate capability of the $NiFe_2O_4/Fe_2O_3$ nanotubes anode.

capacities are 1488.4 and 1045.2 mAh g^{-1} for $NiFe_2O_4$, and 1400.9 and 989.1 mAh g^{-1} for $NiFe_2O_4/Fe_2O_3$. The large irreversible capacity loss in the first cycle could be ascribed to the irreversible decomposition of the electrolyte and the formation of SEI film.[27]

Fig. 8c shows the capacity and Coulombic efficiency *vs*. cycle number profile of the $NiFe_2O_4/Fe_2O_3$ nanotubes at a current density of 100 mA g^{-1} in the voltage range of 0.01-3 V. It is found that the discharge capacity of $NiFe_2O_4/Fe_2O_3$ with slight drop in the charge-discharge process, indicating the excellent cycling stability of the composite. A high reversible capacity of 936.9 mAh g^{-1} could still be achieved even after 100 charge-discharge cycles. Furthermore, the Coulombic efficiency shows a rapid increase to 96% after the second cycle and keeps stable around 98% in the subsequent cycles. For comparison, under the identical test conditions, the $NiFe_2O_4$ exhibits a rapid decay of capacity, and a capacity of only 598.1 mAh g^{-1} is left after 100 cycles. (Fig. S6b).

In addition to the high specific capacity and excellent cycling stability, the rate capability is another crucial property for high performance LIBs. Fig. 8d gives the rate capability of the $NiFe_2O_4/Fe_2O_3$ nanotubes at progressively increased current density. The $NiFe_2O_4/Fe_2O_3$ exhibits decent capacity retention with the average discharge capacity of 1392.9, 1079.7, 812.5, 586.7, 423.6 mAh g^{-1} at current density of 100, 200, 500, 1000 and 2000 mA g^{-1}, separately. Even at the rigorously high current density of 5000 mA g^{-1}, a discharge capacity of 193.2 mAh g^{-1} could still be delivered. More importantly, a high discharge capacity of 1070.3 mAh g^{-1} could be resumed when the current density returns to 100 mA g^{-1}. This demonstrates the great potential of $NiFe_2O_4/Fe_2O_3$ nanotubes as high-rate anode materials for LIBs.

It is obvious that the $NiFe_2O_4/Fe_2O_3$ nanotubes exhibit superior electrochemical performance, which can be explained by the following factors. Firstly, the hierarchical porous one dimensional structures can improve the electrochemical kinetics effectively: shorten the transport length of lithium ion and electron, offer large electrode-electrolyte interface, reduce the

diffusion length and resistance of the electrolyte molecules.[8] Secondly, the hollow tube structure can relax the stress caused by volume change during the charge-discharge process, thus maintaining the mechanical integrity and chemical stability of the electrode materials.[21] Finally, the richer redox chemistry and the synergetic effect of nickel and iron ions may also contribute to the better electrochemical performance.[12-14]

Conclusions

In summary, this work reports a facial method for the controllable preparation of hierarchical porous $NiFe_2O_4/Fe_2O_3$ nanotubes by using core/shell Fe_2Ni MIL-88/Fe MIL-88 nanorods as template. When evaluated as anode materials, the $NiFe_2O_4/Fe_2O_3$ nanotubes exhibit large reversible charge-discharge capacity, excellent cycling stability and superior rate capability. The hierarchical porous nanotube structures and the synergetic effect of $NiFe_2O_4$ and Fe_2O_3 may contribute to the improved electrochemical performance. Furthermore, MOFs-template synthesis of metal oxide is an effective technique for preparing porous materials with rationally designed structures and hold promising for the fabrication of high performance anode materials for advanced LIBs.

Acknowledgements

This work is supported by the National Nature Science Foundation of China （Grant No. 20111061）.

Notes and references

[a] State Key Laboratory of Rare Earth Resource Utilization, Changchun Institute of Applied Chemistry, CAS, Changchun, 130022, China. Email: lmwang@ciac.ac.cn, Tel: +86-431-85262447, Fax: +86-431-85262836.
[b] Changzhou Institute of Energy Storage Materials and Devices, Changzhou 213000, China.
[c] University of Chinese Academy of Sciences, Beijing 100049, China.
Electronic Supplementary Information (ESI) available: [details of any supplementary information available should be included here]. See DOI: 10.1039/b000000x/

1 M. Armand and J. M. Tarascon, *Nature*, 2008, **451**, 652.
2 R. Mukherjee, A. V. Thomas, A. Krishnamurthy and N. Koratkar, *ACS Nano*, 2012, **6**, 7867.
3 M. Du, C. H. Xu, J. Sun and L. Gao, *J. Mater. Chem. A*, 2013, **1**, 7154.
4 S. Wu, Z. Y. Wang, C. N. He, N. Q. Zhao, C. S. Shi, E. Z. Liu and J. J. Li, *J. Mater. Chem. A*, 2013, **1**, 11011.
5 L. Y. Pan, H. B. Zhao, W. C. Shen, X. W. Dong and J. Q. Xu, *J. Mater. Chem. A*, 2013, **1**, 7159.
6 Q. Hao, J. P. Wang and C. X. Xu, *J. Mater. Chem. A*, 2014, **2**, 87.
7 L. Yu, H. B. Wu and X. W. Lou, *Adv. Mater.*, 2013, **25**, 2296.
8 Z. Y. Wang, D. Y. Luan, S. Madhavi, C. M. Li and X. W. Lou, *Chem. Commun.*, 2011, **47**, 8061.
9 Y. S. Fu, Y. H. Wan, H. Xia and X. Wang, *J. Power Sources*, 2012, **213**, 338.
10 Y. L. Xiao, J. T. Zai, L. Q. Tao, B. Li, Q. Y. Han, C. Yu and X. F. Qian, *Phys. Chem. Chem. Phys.*, 2013, **15**, 3939.
11 J. H. Sui, C. Zhang, D. Hong, J. Li, Q. Cheng, Z. G. Li and W. Cai, *J. Mater. Chem.*, 2012, **22**, 13674.
12 X. Gu, L. Chen, Z. Ju, H. Xu, J. Yang and Y. Qian, *Adv. Funct. Mater.*, 2013, **23**, 4049.
13 H. Wu, M. Xu, Y. Wang and G. Zheng, *Nano Res.*, 2013, **6**, 167.
14 W. Zhou, C. Cheng, J. Liu, Y. Tay, J. Jiang, X. Jia, J. Zhang, H. Gong, H. H. Hng, T. Yu and H. J. Fan, *Adv. Funct. Mater.*, 2011, **21**, 2439.
15 L. Ge, W. Zhou, V. Rudolph and Z. H. Zhu, *J. Mater. Chem. A*, 2013, **1**, 6350.
16 P. Ju, L. Jiang and T. B. Lu, *Chem. Commun.*, 2013, **49**, 1820.
17 Q. L. Zhu, J. Li and Q. Xu, *J. Am. Chem. Soc.*, 2013, **135**, 10210.
18 J. W. Cao, Y. F. Gao, Y. Q. Wang, C. F. Duan and Z. L. Liu, *Chem. Commun.*, 2013, **49**, 6897.
19 L. Zhang, H. B. Wu, S. Madhavi, H. G. Hng and X. W. Lou, *J. Am. Chem. Soc.*, 2012, **134**, 17388.
20 B. Liu, X. B. Zhang, H. Shioyama, T. Mukai, T. Sakai and Q. Xu, *J. Power Sources*, 2010, **195**, 857.
21 L. Hu, Y. M. Huang, F. P. Zhang and Q. W. Chen, *Nanoscale*, 2013, **5**, 4186.
22 C. C. Li, X. M. Yin, L. B. Chen, Q. H. Li and T. H. Wang, *Chem. Eur. J.*, 2010, **16**, 5215 .
23 X. H. Cao, B. Zheng, X. H. Rui, W. H. Shi, Q. Y. Yan and H. Zhang, *Angew. Chem. Int. Ed.*, 2013, **52**, 1.
24 X. D. Xu, R. G. Cao, S. Jeong and J. Cho, *Nano Lett.*, 2012, **12**, 4988.
25 G. –T. Vuong, M. –H. Pham and T. –O. Do, *Dalton Trans.*, 2013, **42**, 550.
26 W. Cho, S. Park and M. Oh, *Chem. Commun.*, 2011, **47**, 4138.
27 J. Lin, A. –R. O. Raji, K. W. Nan, Z. W. Peng, Z. Yan, E. L. G. Samuel, D. Natelson and J. M. Tour, *Adv. Funct. Mater.*, **DOI**: 10.1002/adfm.201303023.
28 Q. Q. Xiong, J. P. Tu, X. H. Xia, X. Y. Zhao, C. D. Gu and X. L. Wang, *Nanoscale*, 2013, **5**, 7906.
29 J. X. Zhu, D. Yang, X. H. Rui, D. H. Sim, H. Yu , H. H. H. H. E. Hoster, P. M. Ajayan and Q. Y. Yan, *Small*, 2013, **9**, 3390.
30 H. X. Zhao, Z. Zheng, K. W. Wong, S. M. Wang, B. J. Huang, D. P. Li, *Electrochem. Commun.*, 2007, **9**, 2606.
31 C. Y. Wu, X. P. Li, W. S. Li, B. Li, Y. Y. Wang, Y. T. Wang, M. Q. Xu, L. D. Xing, *Journal of Power Sources*, 2014, **251**, 85.
32 Z. C. Bai, Z. C. Ju, C. L. Guo, Y. T. Qian, B. Tang, S. L. Xiong, *Nanoscale*, **DOI:** 10.1039/C3NR05676G.

